Neural computation through sensorimotor dynamics for predictive sensorimotor control

Running Title: Sensorimotor neural dynamics in motor cortex

Yiheng Zhang[1,3,4], Yun Chen[1,3,4], Tianwei Wang[1,3], and He Cui[1,2,3]*

[1] Center for Excellence in Brain Science and Intelligence Technology, Institute of Neuroscience, Chinese Academy of Sciences, Shanghai 200031, China

[2] Chinese Institute for Brain Research, Beijing, 102206, China

[3] University of Chinese Academy of Sciences, Beijing 100049, China

[4] equal contributions

*Correspondence: hecui@cibr.ac.cn

Abstract

Although recent studies suggest that activity in the motor cortex conveys substantial information regarding sensory inputs in addition to motor outputs, it is unclear how sensory inflows affect the motor outflows issuing motor commands. Here, we recorded population neural activity in the motor cortex via microelectrode arrays while monkeys performed flexible manual interception of moving targets. For this task, which requires predictive sensorimotor control, the activity of most neurons in the motor cortex not only encoded upcoming movements, but was also influenced by ongoing target motion. Dimensionality reduction at movement onset demonstrated a latent orbital neural geometry with neural states clustered by reach directions, and tilted in ellipses corresponding to target speed. This neural geometry was investigated by our representational model and recurrent neural network (RNN) with task-specific input-output mapping. We propose that neural computation through sensorimotor dynamics can be derived from the neuronal mixed sensorimotor selectivity and dynamic interaction between modulations.

Introduction

Motor cortex, a brain region generating motor commands, is widely known for its relation to movement kinetics[1,2] and kinematics[3–5]. Moreover, it has been reported to also carry substantial sensory information[6–12]. Activity in the motor cortex can be strongly influenced by reference frame[13], hand trajectory[14], and stimuli for target selection[15]; there even exists evoked activity during visual replay related to the tracking movements[16]. However, it is yet unclear how sensory inflows affect motor-output neural dynamics in the motor cortex.

With recent advances in large-scale neural recording and population analysis, the dynamical systems perspective, which posits the motor cortex as an autonomous dynamical machine[17–19], is experiencing a revival in motor control. From this point of view, preparatory population activity is promoted toward a movement-specific optimal subspace to set initial states seeding the motor generation[20,21]. However, it remains to be determined if the initial states for generating movements would be placed in accordance with sensory variables.

To reveal neural dynamics shaped by concurrent sensorimotor signals, we recorded population activity in the primary motor cortex (M1) from monkeys performing a flexible manual interception task. Unlike previous studies requiring interception at a fixed location[9,22], this flexible interception depends on predictive spatiotemporal mappings to displace a body effector to a trial-varying location. We found that the activity of most neurons was jointly tuned to both reach direction and target motion via gain modulation, directional selectivity shifting, offset adjustment, or their combinations. Strikingly, such mixed sensorimotor selectivity exists throughout the entire trial, in contrast to the gradient of sensory-to-motor tuning from cue to movement epochs that we recently reported in posterior parietal cortex (PPC)[23]. Principal component analysis (PCA) of the neural population revealed a clear orbital neural geometry in low-dimensional space at movement onset. Interestingly, the neural states were distributed in reach-direction order, and formed ringlike structures whose slopes were determined by target-motion conditions. Neuronal simulation indicates that these characteristics of neural population dynamics could be derived from the mixed sensorimotor selectivity of single neurons. A recurrent neural network (RNN) trained with proper input-output mappings offers insight into the relationship between neuronal modulation and neural geometry in a dynamical system. We propose sensory modulation of preparatory activity at both single-neuron and population level as general element of neural computations for predictive sensorimotor control.

Results

Behavioral task and performance

Three monkeys (*Macaca mulatta,* C, G, and D, male, weight 7 to 10 kg) were trained to perform a delayed manual interception task (Fig. 1a), which was modified from that used in our recent studies[23,24]. To initiate a trial, the monkey needed to hold a dot in the center of a standing touch screen for 600 ms. Then, a peripheral target appeared, either stationary or in circular motion around the center dot at a constant angular speed. The monkey was required to wait for a random delay (400-800 ms) until the central dot went dark (GO) to immediately reach to the target. Once the monkey touched any peripheral location (Touch), the target stopped and another dot appeared at that location, colored red for a successful interception or blue for a failure. The error tolerance between target and touched location (endpoint) was 3 cm. There were five target-motion conditions, consisting of clockwise (CW) conditions -240 °/s and -120 °/s, counterclockwise (CCW) conditions 120 °/s and 240 °/s, along with 0 °/s (static target) condition. We define the target-speed magnitude as TS_{mag} (0 °/s, 120 °/s, and 240 °/s) and the target-speed direction as TS_{dir} (CCW and CW). These target-motion conditions were interleaved trial by trial, and the location of the initial target was random.

In order to facilitate the analysis of directional tuning, as in a previous study[24] we divided the circular space equally into eight sectors, and grouped trials according to the angle of reach endpoint. For well-trained monkeys, the reach was launched directly toward the target location at interception, with little in-flight adjustment (Fig. 1b) as[24]. The behavioral performance across the five target-motion conditions was largely consistent, with overlapped endpoint distribution (Fig. 1b dot ellipses) and similar hand velocity profiles (Fig. 1c, correlation coefficient of mean hand velocity profile in five target-motion conditions during GO to Touch is 0.96 ± 0.05, mean ± sd. for eight sectors). For monkey C, the peak hand velocities varied with TS_{mag} but not TS_{dir} (12.4 ± 2.3, 11.5 ± 1.6, 11.1 ± 2.1, 11.7 ± 2.6, and 13.2 ± 3.6 cm/s, mean ± sd. for -240 °/s, -120 °/s, 0 °/s, 120 °/s, and 240 °/s conditions, respectively; Kruskal-Wallis test, multi-comparison $p < 10^{-11}$ among five target-motion conditions, but $p > 0.1$ for comparison between -240 °/s and 240 °/s, or between -120 °/s and 120 °/s), and there was a tendency of faster target speed inducing faster peak hand velocity (correlation of TS_{mag} and the peak hand velocity is 0.24, $p < 10^{-12}$, including 772 trials). The behavioral statistics of three monkeys are shown in Fig. S1.

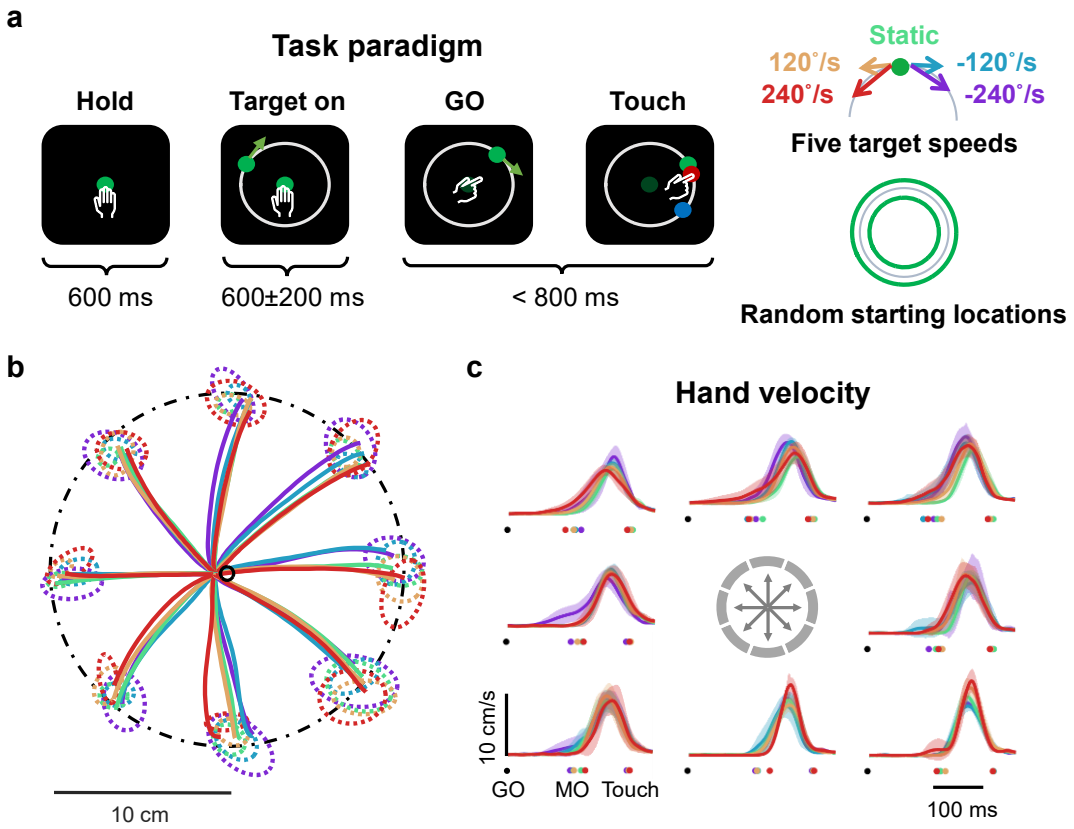

Fig. 1: Flexible manual interception task and behavioral performance
a Diagram of interception task. The five target- motion conditions (-240°/s, - 120°/s, 0°/s, 120°/s, and 240°/s) are indicated in five colors (purple, blue, green, yellow, and, red). Target starting location was randomly distributed.
b The condition-averaged hand trajectory. The mean trajectories from GO to touch in five target motion conditions (monkey C, 772 correct trials in one session) are plotted as solid lines in the same color as in [**a**, **b**]. Reach direction was divided into eight zones each covering 45 degrees, and represented by the corresponding eight directions. The distribution of reach endpoints relative to target location at interception are shown by the dot ellipses. The shifted center-holding is likely due to individual preference.
c The condition-averaged hand velocity. Hand velocity in the same session was averaged by both target speed and reach direction as in [**b**]. The lines are in the same color as in [**a**] and the position of subplots corresponds to the reach direction denoted by gray inset. All profiles are aligned to GO (black dots) with marked movement onset (MO) and touch (interception) time (dots in colors).

Mixed sensorimotor selectivity of single neurons
Our next question is whether the directional selectivity of neurons in the motor cortex is modulated by target speed. To this end, we recorded single neurons with Utah arrays from monkey C, G, and D (implanted sites were shown in Fig. 2a, and all datasets listed in Table S1) during the interception task.

Notably, we found that neuronal directional tuning during the execution period was affected by target motion, mainly in three ways according to our statistical criteria: preferred direction (PD) shift modulation, gain modulation, and addition modulation (Fig. 2b and Fig. S2-S4, Methods). PD-shift neurons had their PDs shifted in moving-target conditions compared to the PDs in the static-target condition. In this case, TS_{dir} rather than TS_{mag} dominated the modulation, as illustrated by an example neuron (Fig. 2b, *PD shift*): its PDs corresponding to CCW conditions (red and yellow) and CW conditions (blue and purple) exhibited obvious distinction. Gain-

modulation neurons exhibited reach-direction tuning multiplied by target speed: while their directionality remained invariant, the neuronal responses at PD differed across target-motion conditions. This modulation was overarched by TS_{dir} as well. The turning curves of the example neuron (Fig. 2b, *gain*) had higher responses at PD in CW conditions (blue and purple) than in others (green, yellow, and red), indicating a varying tuning depth for reach direction. Neurons with addition modulation underwent changes of offset activity induced by target speeds (both TS_{dir} and TS_{mag}). As with the example neuron (Fig. 2b, *addition*), this effect was almost equal for all reach directions.

Nevertheless, it was difficult to classify all neurons with mixed sensorimotor selectivity into one of these three groups exclusively, because many of them experienced a mixture of two or three of above modulations (Fig. 2c). Moreover, the proportions of three groups were almost equal, and there was no obviously anatomical clustering, making it a challenge for further analytical description at the single-neuron level.

These target-motion modulations of neuronal directionality tuning are largely dominated by TS_{dir}, the target rotation direction, rather than $TS_{mag,}$ the target speed magnitude, related to the peak hand velocity, which suggests the participation of sensory signals in shaping neural dynamics during interception execution.

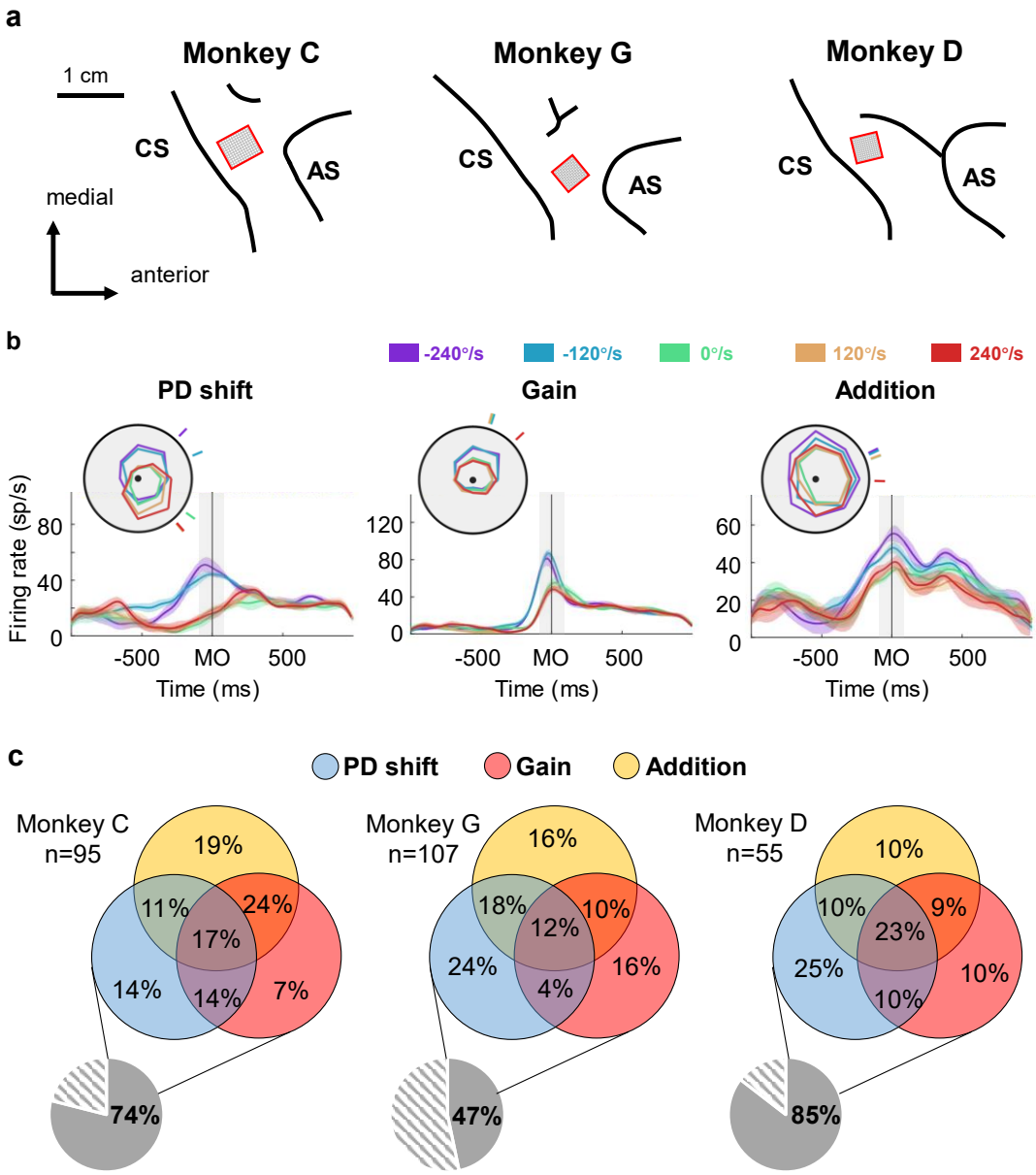

Fig. 2: Mixed sensorimotor selectivity of single neurons
a Implanted locations of microelectrode array in the motor cortex of the three monkeys. Neural data were recorded from monkeys using the hand contralateral to the recorded cortical regions. AS, arcuate sulcus; CS, central sulcus.
b Three example neurons with PD shift, gain modulation, and offset addition. The peri-stimulus time histograms (PSTH) show the activity of example neurons when monkeys reached to upper areas in five target motion conditions. The shadow area of PSTH lines denotes the standard error of trials. The inset as polar plot shows the movement-tuning curves (average firing rate of eight reach-endpoint sectors are colored in five target-motion conditions) in polar coordinate system around the movement onset (± 100 ms), with surrounding short bars pointing to the preferred directions.
c The proportions of three types of modulation around MO of three monkeys. The small pie charts show the proportions of neurons with (gray) or without (shadow) sensory modulation. The large pie charts show the proportions of neurons with mixed sensorimotor selectivity specifically in PD shift (blue), gain modulation (red), offset adjustment (yellow), or their mixture (overlapped).

Population decoding sensory and motor information

To learn more about the effect of target motion on interception, we analyzed the neural dynamics at the population level.

We first performed a decoding analysis to verify the temporal pattern of neuronal population activity conveying the information of target motion and reach direction. Here, neural data in a sliding window was utilized to train a support vector machine (SVM) classifier for target-motion conditions (one in five), and another for reach directions (one in eight) as control (Methods). As Fig. 3a shows, the decoding accuracy of the target-motion condition rose quickly and peaked at over 70% around GO, while the decoding accuracy of reach direction climbed and reached a plateau of about 80% before movement onset (MO). These results suggest that, during almost the entire trial, motor outflow co-exists with sensory inflow in M1.

A question rises as whether the neural population response for motor output was also modulated by target motion, so we conducted another decoding analysis to compare the similarity of coding rules across conditions. For reach direction decoding (Fig. 3b left), the color of each patch denotes the decoding accuracy of the decoder trained by the column data and tested with the row data (Methods). Specifically, the decoder was expected to reveal reach direction under row target-motion conditions, either trained by the column data from the same target-motion condition or from others. It turned out that the reach-direction decoder could be generalized between static-target and moving-target conditions at GO and MO. This generalization, however, held only for the conditions with the same TS_{dir} (within CCW conditions or CW conditions), but not for those conditions across opposite TS_{dir} (the decoder for CCW conditions couldn't apply to CW conditions, and vice versa). We obtained the confusion matrix of decoding target-motion conditions in a similar way (Fig. 3b right), but this decoder only showed temporal generalization between TO-GO and GO-MO, and was poorly generalized across the other reach directions.

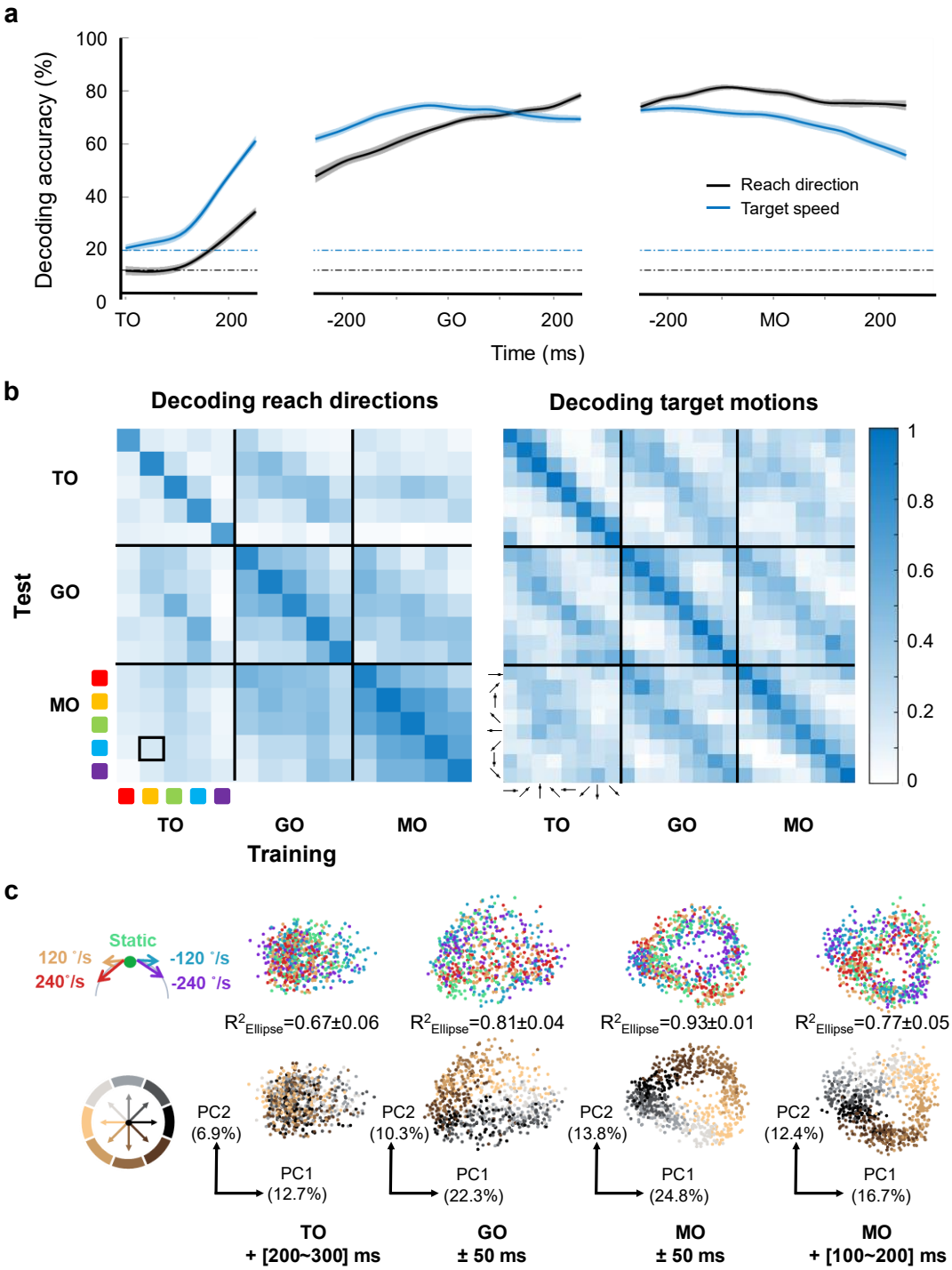

Fig. 3: Features of encoding pattern at population level

a The mean accuracy (SVM with 10-fold cross-validation) of decoding reach direction (black solid line) and target speed (blue solid line) for population activity (monkey C, n=95, 100-ms window sliding at 50-ms step), aligned to target on (TO), GO, and MO. The black and blue dash-dotted lines are chance levels for reach direction (one in eight) and target speed (one in five), respectively. The shaded area is the standard deviation of ten repetitions.

b The accuracy of decoding reach direction and target speed in different conditions (the same dataset in Fig. 3a). The left panel shows the accuracy of decoding reach direction among five target-motion conditions in three epochs: [200-400] ms after TO, GO ± 100 ms, and MO ± 100 ms (SVM with 10-fold cross-validation, and the chance level is 1/8). The five target-motion conditions are labeled in

five colored squares (the same color rule as Fig. 2b). The abscissa represents the training data order of target-motion condition during one epoch, and the ordinate is the test data arranged in a consistent order. For example, the framed patch corresponds to a classifier trained by data in 120 °/s during TO and tested by -120 °/s during MO. The decoding accuracy is shown by the color depth. The right panel shows the decoding accuracy of target motions in distinct reach directions and time windows (SVM with 10-fold cross-validation, the chance level is one in five) with arrows with different direction indicating the reach direction.
c The neural states in different time windows. In the space spanned by the first two principal components (PCs), each point represents the neural state of a single trial, and is colored in target speed (top) or reach direction (bottom). The corresponding explained variance of PCs and the R^2 of fitting ellipses is marked for different epochs.

To explore the modulation rules of sensory inflow changing neural dynamics while preserving motor outflow, we performed principal component analysis (PCA) on the normalized population activity. Fig. 3c shows the neural states of single trials in different time windows. As MO approached, neural states gradually clustered by reach direction. The first two principal components (PCs) of the neural states at MO explained the most variance ([24.8%, 13.8%]), and were most related to reach direction (the mean fitting goodness of reach direction, $[R^2_{pc1}, R^2_{pc2}]$ = [0.93, 0.86]). Furthermore, the neural states tended to form ringlike structures at MO (the goodness of fitting ellipses R^2 = 0.67 ± 0.06, 0.81 ± 0.04, 0.93 ± 0.01, and 0.77 ± 0.05, in the four epochs, mean ± sd. across five target-motion conditions). This inspired us to consider the possibility that the neural dynamics in M1 encoding reach direction were subjected to topologically invariant geometric transformation by target motion at MO.

Orbital neural geometry in latent space

Next, we concentrated on the newfound neural geometry in low-dimensional space at MO to examine the modulated neural states. We projected all neural states into the three-dimensional subspace resulted from zero target-speed condition (Fig. 4a and Fig. S5). The projections of the single-trial neural state onto the PC1-PC2 subspace clustered, or rather distributed, in reach-direction order (Fig. 4a top and Fig. 4b right). Interestingly, the interlocked ringlike structures in two-dimensional space disengaged from each other in three-dimensional space, and the 'target-motion tiltings', which were the angles between ellipses fitting from neural states under single target-motion conditions (the fitting goodness of ellipses, R^2 = 0.92 ± 0.01, ellipse eccentricity = 0.59 ± 0.11, mean ± sd. across five target-motion conditions, see Methods), exhibited concentric shapes. Furthermore, these ellipses tilted at condition-dependent angles, which is particularly evident in the PC2-PC3 subspace (Fig. 4a bottom and Fig. 4b left). To manifest the potential representation of target-motion information, we quantified the spatial features of these ellipses by calculating the elevation and azimuth angles of their normal vectors. As Fig. 4c, the elevation angles are related to TS_{mag}, whereas the azimuth angles were determined basically by TS_{dir}. We also computed the between-ellipse angles, which were the angles between ellipses of the moving-target and static-target conditions. Strikingly, this relative angle was linearly correlated with target speed (both TS_{mag} and TS_{dir}), and the relationship was robust in nine datasets from three monkeys (Fig. 4d).

Given these results, we propose that this orbital neural geometry, including both the target-motion titling and the reach-direction ellipses, epitomizes the sensorimotor dynamics of M1 at population level. The sensory input can regularly modulate neural states in an orthogonal dimension (PC3), without interfering with motor generation (in PC1 and PC2).

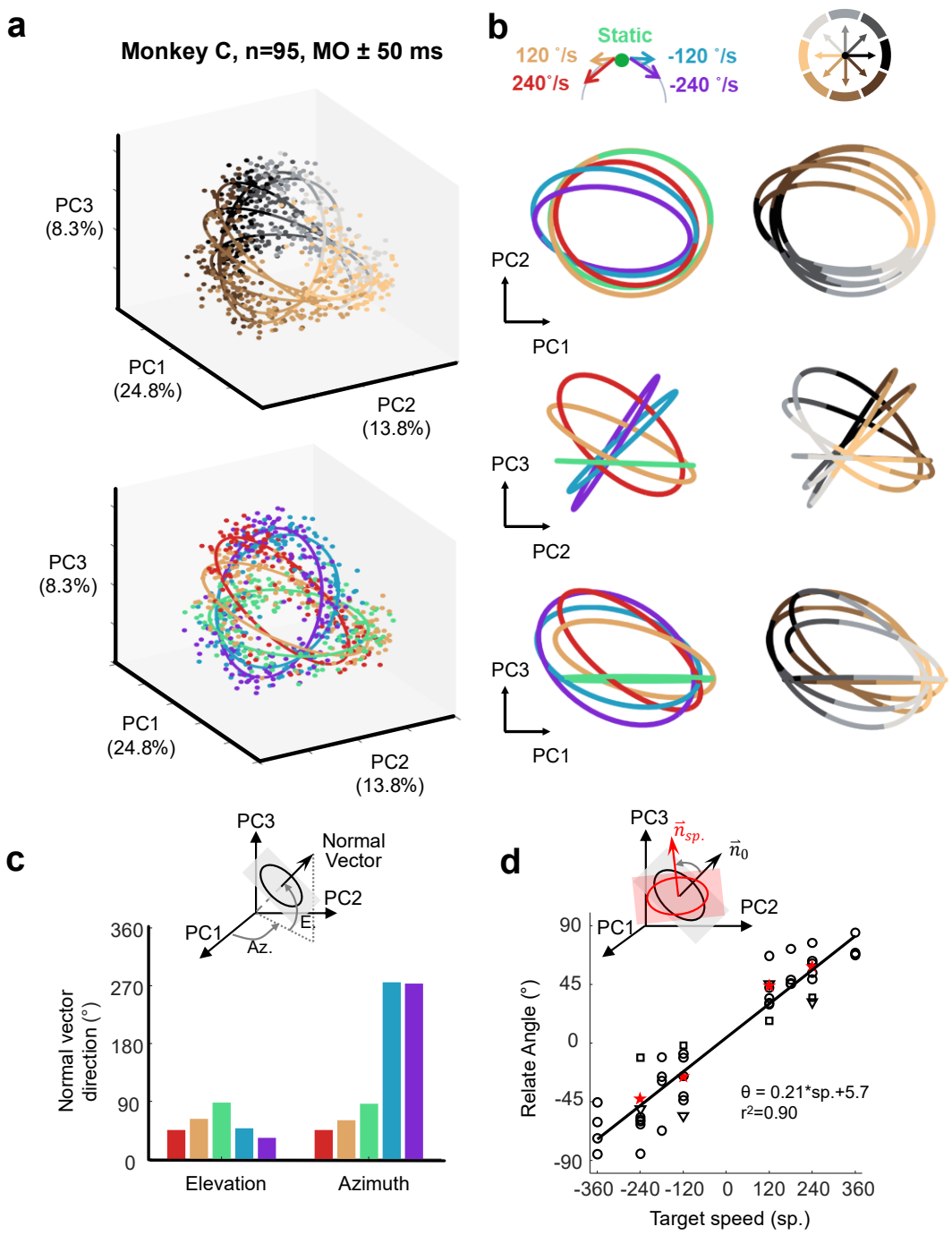

Fig. 4: The orbital neural geometry in latent dynamics

a Three-dimensional neural state of M1 activity obtained from PCA. As in Fig. 3c, each point represents a single trial. The upper subplot is colored according to five target speeds, while the bottom is in colors corresponding to eight reach directions. The explained variances of the first three PCs were 25.6%, 14.7%, and 8.7%.

b Fitted ellipses of neural states. The ellipses fitted in [**a**] are projected onto three two-dimensional spaces, colored in target speeds (left column) or reach directions (right column).

c Elevation and azimuth angle of normal vectors of the fitted ellipses in [**a**].

d The relative angle of ellipses. The angle is calculated between ellipses of target-motion condition and static-target condition (0 °/s) in the range from -90° to 90°, CCW is positive. The red pentagrams are example session in [**a-c**]. Circles are the other six sessions from monkey C, and squares and triangles are from one session of monkey G and D, respectively (more detail in Table S1). The line

represents the linear relationship of ellipses angle (θ) and target speed (sp.) in nine sessions, with function $\theta = 0.21*sp.+5.7$, $R^2=0.90$.

Population neural geometry relies on neuronal tuning

Presumably, the geometry of neural states is rooted in neuronal mixed sensorimotor selectivity, so we probed whether a group of single neurons with some type of mixed sensorimotor selectivity could exhibit the neural geometry instantaneously.

For this purpose, three models for single neurons were deduced from the three typical modulations described above (PD shift, gain, and addition, see Fig. 2 and Fig. S2-S4), along with a full model designed to contain them all (Methods). We found that the adjusted R^2 of the full model (0.64 ± 0.21, mean ± sd. across neurons, similarly hereinafter) was larger than that of the PD shift (0.59 ± 0.23), gain (0.56 ± 0.21), and addition (0.47 ± 0.24) models for monkey C (n=95, rank-sum test, $p<0.01$, see examples in Fig. 5a, Fig. S6). The results were similar for all three monkeys (Fig. S6), in line with the mixture of patterns of sensorimotor selectivity of single neurons.

Next we ran a simulation with these representational neuronal models. To clarify the effect of each modulation, we performed PCA on the activity of three groups of model neurons (Fig. 5b). Here, each group consisted of 200 model neurons with their PDs uniformly distributed, and was solely modulated as PD-shift, gain, or addition (Methods). The resulting neural geometry of the three simulation groups showed distinct features (Fig. 5c): The reach-direction ellipses were inclined with target-motion-dependent angles in the PD-shift and gain groups, similar to the real neural data, but the ellipses in the addition group were layered in parallel. The reach-direction clusters in the first two PCs were preserved in the gain and addition group, but not in the PD-shift group. Taken together, these results indicate that it was the gain modulation group that could exhibit the desired orbital neural geometry.

Nonetheless, we found that a population with a uniform mixture of all three modulations were able to simulate the neural geometry as well (Fig. 5d). This means that the existence of PD-shift and addition modulation would not disrupt the neural geometry driven by gain modulation, reflecting the actual comparable proportions of modulation types.

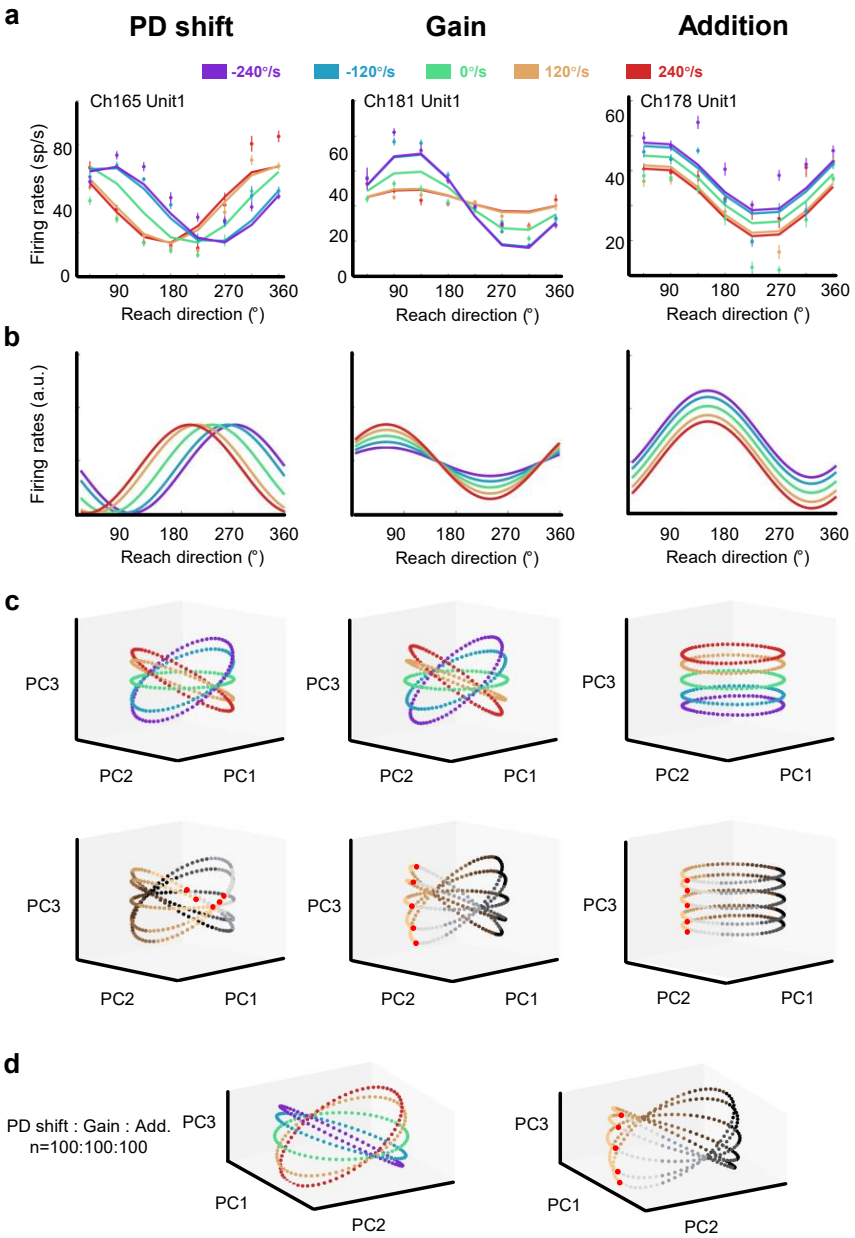

Fig. 5: The shape of neural dynamics relies on neuronal mixed selectivity
a The activity of three example neurons with PD shift, gain, and addition modulation (the same neurons as in Fig. 2b). Dots and bars denote the average and standard error of firing rates, respectively, colored as target-motion conditions. Lines show the fitted firing rates for corresponding models.
b The tuning curves of the three simulated neurons fitted by PD shift, gain, and addition models.
c Neural states of population simulated neurons are shown in the space spanned by the first three PCs, colored by target speed (upper row) or reach direction (lower row). Each population consists of 200 simulated neurons. The neural state in the 180° reach direction is highlighted with a red marker. The first two PCs can explain more than 95% of the variance in the data (explained variance for the first three PCs, in PD shift: 50.1%, 47.1%, 1.6%; in Gain: 49.5%, 46.6%, 2.0%; in Addition: 50.8%, 47.9% & 1.4%).
d The simulation of PCA for 100 neurons each of three modulation types. The neural state of the mixed population also shows reach clustering in the first two PCs and target-motion tilting in the third PC (explained variance for the first three PCs: 48.7%, 45.8%, and 5.4%), which is similar only to the gain neurons simulation and results form the real data.

Recurrent Neural Network provides dynamic insights

The direct link of single-neuron selectivity to the structure of the population neural states, as exhibited by our simulations, suggests a critical function of gain modulation in a static and assembled way. However, does it signify that the other two types of neural modulations are dispensable? What if the modulated subpopulations are recurrently connected and their dynamics evolve with time?

We built an RNN model to simulate this situation in a dynamical system with interconnected units (Fig. 6a; see Methods). Three kinds of inputs were designed for the network to cover the motor-planning, sensory, and timing inflow. These inputs included motor intention, target location, and Go signal: the former two were represented by two-dimensional Cartesian coordinates, while the GO-signal was a one-dimensional step function. This network was to generate hand velocity in the same two-dimensional cartesian coordinate after MO. The trained network model performed well (mean square error of touch endpoint and target was 0.0024 ± 0.0013, a. u., mean ± sd. across 500 trials, while the radius of target motion was 0.15).

In this network model, we found comparable features of nodes. First, most activated nodes (for example, Fig. 6b) could be classified into the above-mentioned three modulations (Fig. 6c) by the same statistical standard as for neural data. Second, the states reduced from node population activity were arranged in a way resembling the actual neural geometry at MO (the fitting goodness of ellipses, $R^2 = 0.99 \pm 0.00$, ellipse eccentricity = 0.28 ± 0.11, mean ± sd. across five target-motion conditions; Fig. 6d). The elevation and azimuth angles, as well as the between-ellipse angles, all followed the same pattern as suggested by the actual results (Fig. 6e and Fig. 6f blue triangle). The linear relation between target-speed and angle between-ellipse even maintained for generalized conditions (untrained -210 °/s, -180 °/s, -90 °/s, -60 °/s, 80 °/s, 100 °/s, 150 °/s, and 270 °/s, Fig. 6f orange dot), indicating that the mixed tuning may resulted from network properties, and that the ringlike structures could emerge from dynamical evolution.

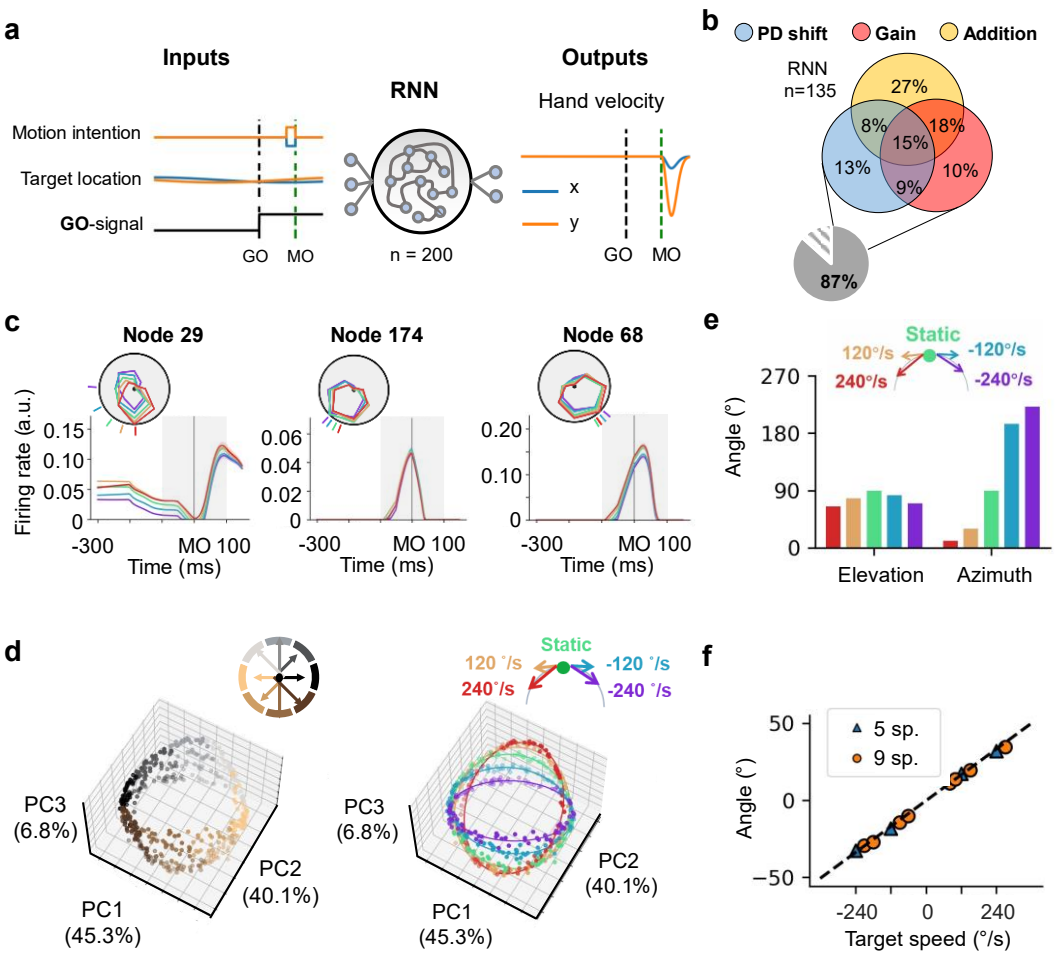

Fig. 6: The neural geometry in RNNs

a Network architecture. The network input consists of motor intention, target location, and GO signal. The motor intention is the two-dimensional Cartesian coordinates of the interception location, the target location is the two-dimensional Cartesian coordinates of the moving target, and the GO-signal is a step function from 0 to 1 after GO. The RNN with 200 hidden units is expected to output hand velocity as two-dimensional Cartesian coordinates for accurate interception.
b The proportions of three types of modulation around MO of the activated nodes. Similar to Fig. 2c.
c Three example nodes with PD-shift modulation, gain modulation, and addition modulation. Similar to Fig. 2b.
d Three-dimensional state of the RNN nodes resulting from PCA. MO-100 ms to MO. Similar to Fig. 3a. Five hundred trials are included and the explained variance of the first three PCs is 45.3%, 40.1%, and 6.8%.
e Elevation and azimuth angle of normal vectors of the fitted ellipses in [**d**]. Similar to Fig. 3c.
g The relative angle of ellipses. Similar to Fig. 3d. The blue triangles are of the situation with trained target speeds: -240 °/s, -120 °/s, 0 °/s, 120 °/s, and 240 °/s; while the orange circles show the situation with 0 °/s and eight untrained target speeds: -210 °/s, -180 °/s, -90 °/s, -60 °/s, 80 °/s, 100 °/s, 150 °/s, and 270 °/s. The fitted line is $\theta = 0.14 * sp. - 0.39$, $R^2 = 0.9983$ for five target speeds, and $R^2 = 0.9958$ for nine target speeds.

With this RNN model, we were prepared to tackle the two questions raised at the beginning of this section to examine the contribution of reach subpopulation for neural geometry. We first silenced nodes of certain modulation types (Fig. 7a). The axis of the neural geometry rotated without PD-shift modulation nodes (Fig. 7b), which indicated that the movement coding in PC1 and PC2 had been relegated to PC2 and PC3; while there was

little change in the absence of gain or addition modulation (Fig. S7). We then blocked the connection between different modulation groups. As the connection involving gain modulation was generally stronger (Fig. 7c), blocking the connection from gain to addition nodes would perturb the tilting (Table S2). However, the greatest influence was caused by blocking the connection from addition to PD-shift nodes (Fig. 7d). In this case, the shape formed by node states changed from five tilting ellipses to a unified curved surface, with states not in circular reach-direction order anymore. From these results, the contributions of three modulations in a dynamical and connected group (in RNN) appear to differ with those in a static and parallel group (in the neuronal model simulation). We speculate that the PD-shift modulation guarantees motor-output encoding in the first two PCs, which relies on recurrent interaction between modulations.

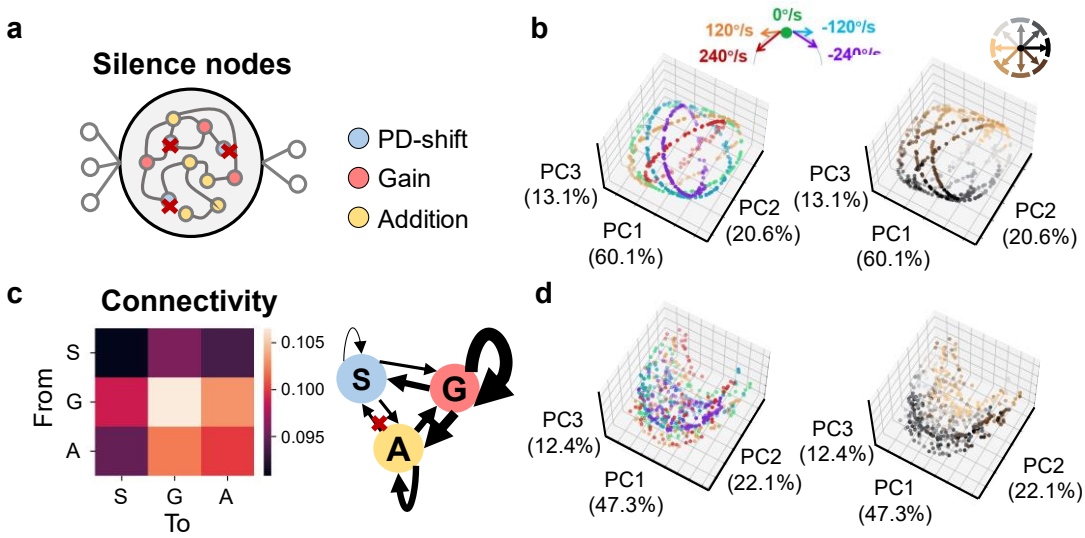

Fig. 7: The perturbed node geometry

a The schematic diagram of silencing nodes. Here the nodes classified as PD-shift modulation are silenced. All connections of this type of nodes are set to zero.

b Three-dimensional state of the RNN nodes with silenced PD-shift nodes. Similar to Fig. 3A. The 500 test trials are the same as Fig. 6d. The explained variance of the first three PCs is 60.1%, 20.6%, and 13.1%.

c The connectivity between different types of modulations. On the left is a heatmap with color representing the averaged absolute connection weight. S for PD-shift nodes, G for gain nodes, and A for addition nodes. On the right is a diagram of the connectivity, with linewidth representing the connection strength. Here, the connection from addition nodes to PD-shift nodes is blocked (set to zero) as marked by the red cross.

d Three-dimensional state of the RNN nodes with blocked connection from addition to PD-shift nodes. Similar to Fig. 3a. The 500 test trials are the same as Fig. 6d. The explained variance of the first three PCs is 47.3%, 22.1%, and 12.4%.

Discussion

To reveal how sensory inflows influence the neural dynamics during motor preparation and execution, we recorded M1 population activity from monkeys performing a flexible manual interception that is highly dependent on predictive sensorimotor transformations. Single-neuron activity showed that the movement tuning of M1 neurons varied with target-motion conditions in complicated ways, including PD shift modulation, gain modulation, addition modulation, or their mixture. Dimensionality reduction on population activity revealed an orbital neural geometry, where neural states formed reach-direction ellipses and tilted by target-motion conditions. Such a geometry, which could be simulated with a group of representational neurons of solely gain modulation, also emerged in the RNN with appropriate input-output mappings. In a dynamic and connected population as the RNN, the PD-shift modulation together with the interactions between modulations were indispensable in preserving the encoding of motor output. These results reveal sensory modulation of neural dynamics during movement at the single-neuron and population levels, and bridge the neuronal mixed sensorimotor selectivity and a low-dimensional neural geometry compactly representing the sensorimotor co-function.

Based on the efficient and systematic dissociation between sensory modulation and motor generation afforded by the behavioral paradigm[24], the adopted delayed interception task links the circularly moving target and the predictive center-out reach, thus disclosing the effect of target-motion on movement-directional tuning. The resulting movement endpoints distributed over the entire circle in our task enabled further scrutiny of the interaction between sensory and motor information, compared to those limited to a fixed touch point[25]. In addition, the regular target motion in our task resulted in similar behavioral characteristics, as opposed to the winding hand trajectories in a random pursuit task[16]. The modulated neural dynamics, though distinguished with target-motion conditions, is ultimately shaped for motor generation rather than sensory representation. Previous studies have showed that M1 is seldom evoked by purely visual stimuli, with only weak tuning[8,26,27], and has transient responses to behaviorally relevant visual cues[7,10,28–30].

Although it has been reported that there are interactions between motor kinematic variables such as reach direction and hand velocity[14,31,32], hand velocity does not fully explain our findings in the neural response: hand velocity varied with TS_{mag}, but neural activity's largest variation was related to TS_{dir}. In addition, if trials with extreme hand velocity were excluded, the orbital neural geometry remained similar, and the target-motion gain model provided a better explanation compared to the hand-velocity gain model (Fig. S8). The motor cortex is also known to reflect kinetic variables like force[1,33,34], so it is a pity that we did not record sufficient muscle data during interception to offer relevant evidence. We do not argue against the possibility that the neural dynamics tends to encode muscular activity, but we believe that such a tendency can be contained in coding for motor generation, which would not invalidate our main proposal.

In the orbital neural geometry, the sensory modulation seems to be embedded in the third PC, whereas the motor information captures the first two PCs (Fig. 4 and Fig. S5). This orthogonality of target-motion information relative to reach direction is consistent with the output-null hypothesis[35], which is also supported by a study explaining how perturbation-evoked responses avoided affecting ongoing movements[36]. Moreover, the maintenance of this neural geometry for more than 200 ms (Fig. 3c, neural states around GO and MO) can be attributed to evolution from different initial states. The initial states are set by preparatory activity in the motor cortex, which is promoted towards a movement-specific optimal subspace[20,21]. Because the motor cortex can be treated as an autonomous dynamical system[17,19], its evolution is influenced by initial states. In this case, the distribution of the

initial states is hinted at by the orbital neural geometry, correspondingly featured by the reach-direction ellipses and the target-motion tilting. Although the neural geometry in the present study looks similar to some previous studies[37–40] at first glance, we did not find neural trajectories to be temporally scaled by target-motion conditions (Fig. S9). Combined with the behavioral data, the sensory information affects the motor plan not by scaling neural activity pattern or behavioral period temporally, as in those studies about timing action, but likely in a time-invariant way.

As reported above, we found sensory modulation on neural dynamics in M1, linked the neuronal mixed selectivity and the population neural geometry in predictive sensorimotor control, and explored subgroup contribution for neural network dynamics. Recently, it has been proposed that the collective dynamics are flexibly shaped by the constitution of neural subpopulations with different selectivity, and are mainly driven by the complexity of the input-output mapping requirement of the performed task[41,42]. This provides an explanation for the differences among the neural geometries of three monkeys: The larger eccentricity (Fig. S5a) and the more compressed structure (Fig. S5b) of the five reach-direction ellipses might both be related to the relatively lower proportion of recorded neurons with mixed selectivity (44% and 52% *vs*. 66%, see Fig. 2c).

While our simulation with the RNN model demonstrates that gain modulation can solely guide the orbital geometry in the population, the results of perturbation analysis suggest that the PD-shift modulation and the interaction between modulations might be essential. In fact, modulations in the form of PD shift and gain have been widely found in the motor cortex and PPC regions contributing to sensorimotor transformation. For example, motor cortex neurons experience gain and PD shift modulation by arm posture[33,43,44]. Neurons in PPC have eye and hand gain fields for a visually-guided reach plan[45–47], integrating target position related to gaze and hand position to form motor intention[48–50]. Therefore, we believe that three types of modulations should all be involved in sensorimotor computation in predictive motor control.

Because the frontal and parietal areas are strongly interconnected and orchestrate many aspects of action planning[51,52], it is widely believed that the PPC plays a key role in the transformation from sensation to motor intention[49]. In particular, area 7a has been reported to convey sensory information after the appearance of stimuli[9], while explicitly conveying intention about the forthcoming movement before interception[23]. Recent studies show interactions of PPC-motor cortex circuity involved in motor planning, spatial transformation and motor selection[53–55]. Thus target-motion information and motor intention could both be provided by the PPC[49,51], and motor intention should be predictive to compensate for sensorimotor delays[56]. The PPC-M1 circuits could transform the visual target location to generate the predictive reach direction[57], which we are going to address in future studies.

Methods

Animals

Three adult male rhesus macaques (monkey C, D, and G, *Macaca mulatta*, 7-10 kg) were used in this study. The monkeys sat in a primate chair to perform the task. The stimuli were back projected onto a vertical touch screen (Elo Touch system; sampling at 100 Hz, spatial resolution <0.1 mm) about 30 cm in front of the monkeys. The hand trajectory was tracked by an optical camera (VICON Inc.) with an infrared marker on the fingertip. All the maintenance and procedures were in accordance with NIH guidelines and approved by the Institutional Animal Care and Use Committee (IACUC) of Institute of Neuroscience, CAS.

Task and behavior

The monkeys were trained to perform a flexible manual interception task in a dark room. The task paradigm was modified based on the visually-guided reaching interception task in a previous study [24]. At the beginning, the monkey held the green center dot of a touch screen for 600 ms to initiate a trial (Fig. 1a). Then, a green target dot appeared at a random location on the surrounding circle (invisible to the monkey) and moved around the center. The center dot turned dark as a GO cue after a random delay (400-800 ms); then the monkey could intercept the target at any moment within 150-800 ms after GO cue. Once any peripheral location was touched, the target stopped. The tolerance range of the touch endpoint for correct trials was less than 3 cm away from the target. The monkey would be rewarded with juice after each correct trial. The target speed of clockwise (CW) -240 °/s, -120 °/s and counterclockwise (CCW) 120 °/s, 240 °/s, as well as 0°/s, was pseudo-randomly interleaved trial by trial. More kinds of target speeds (-360 °/s, -180 °/s, 180 °/s, 360 °/s added) were introduced in the additional sessions (Table S1).

Data collection

After the monkeys were adequately trained for the task (successful rate > 90%). Head-posts were implanted stereotaxically under anesthesia (induced by 10 mg/kg ketamine, then sustained by 2% Isoflurane). After few weeks of recovery and adaptation, the monkeys were implanted with Utah microelectrode arrays (Blackrock Microsystems, Salt Lake City, UT) in the motor cortex of the hemisphere contralateral to the handedness (Fig. 2a, 128-channel array for monkey C, 96-channel array for monkey G and D). The location of recording area referred to Magnetic Resonance Imaging (MRI) and cortical sulcus features. Neuronal activity was recorded via Blackrock Microsystem 256-channel recording system, sampled at 30 kHz. In the selected sessions, we collected 95, 107, and 55 well-isolate units from monkey C, G, and D, respectively.

Peri-stimulus time histograms (PSTHs)

The spike rasters and PSTHs of single neurons are shown in Fig. 2b and Fig. S2-S4. All trials were classified into forty conditions, eight reach-endpoint sectors by five target-motion conditions. Condition-averaged firing rates were calculated with 50-ms bins and smoothed with a Gaussian kernel (standard deviation = 20 ms). The standard error of firing rates was estimated from the 10 bootstrap samples in the trials of corresponding condition.

Classification of neuronal tuning properties

To classify target-motion modulation for single neuron reach-direction tuning, we used the direction-averaged firing rate around movement onset (MO ± 100ms) to calculate three indexes for each target-motion conditions: the preferred direction (PD), the tuning depth, and the offset activity. The PD of each neuron for different target-motion conditions was calculated by the weighted sum of averaged neuronal firing rates in eight reach-direction

sectors. The tuning depth of each neuron was determined by the range (max - min) of firing rates in corresponding target-motion conditions. The offset activity of each neuron was determined by the mean firing rate (MO ± 100 ms) of each target-motion condition.

Based on the PD, tuning depth and offset activity of single neurons, a neuron was classified as 'PD shift', if its PDs were significantly different between interception and static-target condition (Watson-Williams test in circular data, CircStat by[58]); a neuron was classified as 'gain' if its tuning depths were significantly different between interception and static-target condition (two-tailed Wilcoxon signed rand test, $p<0.05$); a neuron was classified as 'offset' if its offset activities were significantly different between interception and static-target condition (two-tailed Wilcoxon signed rand test, $p<0.05$).

Population decoding

The population activity of the motor cortex was used to decode target motion and reach direction by support vector machine (SVM). Neuronal firing rate was soft-normalized as

$$FR_{norm.} = \frac{FR_{raw}}{FR_{max} - FR_{min} + 5}$$

where raw firing rates was divided by the range of firing rates plus five [17]. We trained two SVM classifiers (MATLAB function 'fitcecoc', 10-fold cross-validation) to decode reach direction (one in eight) and target motion (one in five) of single trials in 100-ms window sliding with 50-ms step, respectively (Fig. 3a). The temporal decoding was repeated ten times to obtain the mean and standard deviation of decoding accuracy.

Then, we tested the generalization of reach-direction and target-motion decoders (SVM, MATLAB function 'fitcecoc', 10-fold cross-validation) in different conditions, shown in the two confusion matrices (Fig. 3b). For this purpose, three epochs were selected as 200~400 ms after TO (TO + [200~400] ms), 200 ms around GO (GO ± 100 ms), and 200 ms around MO (MO ± 100 ms), and normalized population activity was averaged in each epoch to predict reach direction and target motion for a single trial. The reach-direction decoder (Fig. 3b left confusion matrix), which was trained by trials in a set of target-motion conditions (five colored squares of the abscissa labeling 240 °/s, 120 °/s, 0 °/s, -120 °/s, and -240 °/s from left to right) and repeated in three epochs (TO, GO, and MO), was tested with trials from other target-motion conditions and epochs (the same order of target-motion arrangement in the ordinate). The leading diagonals of confusion matrices showed the highest decoding accuracy, as the training and testing in the same group of data. Similarly, the target-motion decoder (Fig. 3b right confusion matrix), which was trained by trials in a given reach-direction condition in each epoch, was tested with trials from other reach-direction conditions and epochs (the arrow representing reach directions were arranged in the same way in the abscissa and ordinate).

Neural state

The population activity was stored in NKT datasets, where N, K, and T denote the number of neurons, trials, and time bins, respectively. We averaged T dimension of neural activity in a 100-ms bin (e.g. the two 50-ms bins around MO), and normalized neuronal dimension by Z-score (MATLAB function 'zscore') to get the a K*N dataset. After preprocessing, we used PCA to reduce the dimension from K*N to K*C (C was the number of principal components). Neural states of single trials were colored in target speed or reach direction (Fig. 3c). All ellipses fitting was performed in three-dimensional space. To show the condition-dependent neural structure more clearly, we also projected neural states with the first three components (PC1-3) into the space of static-target condition (Fig. 4). The relative angles were calculated between ellipses of target-motion conditions and static-target condition in each session, defined CW in minus angle and CCW in positive angle. A set of relative angles were

obtained from corresponding conditions in one dataset, and we used the linear regression model to fit all ellipses angles (θ) and target speeds (sp.) in nine sessions (Fig. 4d, dataset in Table S1).

Fitting and simulating single-neuron activity

We used PD shift, gain, offset, and full models to fit neuronal activity, based on cosine tuning. The gain model introduces nonlinear target-speed effects on the amplitude of cosine tuning as:

$$FR = \left(\frac{a_1}{1+e^{-a_2(sp.)}} + c_2\right) * cos(\theta - \theta_{pd}) + c_1$$

where FR is the firing rate at movement onset (MO ± 100 ms). θ and $sp.$ are the reach direction and target speed, respectively. θ_{pd} is the fitted preferred direction of the neuron. a_1, a_2, c_1 are constants to be fitted. Neurons are fitted by single-trial data.

In the PD shift model, the target-speed effects on PDs as:

$$FR = a_1 * cos\left(\theta - \theta_{pd} + \frac{a_3}{1+e^{-a_2(sp.)}}\right) + c_1$$

with the similar symbols to gain model and a new constant a_3.

In the addition model, the target speed adjusts the offset activity:

$$FR = a_1 * cos(\theta - \theta_{pd}) + \frac{a_3}{1+e^{-a_2(sp.)}} + c_1$$

with similar symbols to above models.

The full model integrates all the three above effects:

$$FR = a_1 * cos(\theta - pd_{sp}) + \frac{a_2}{1+e^{-a_2(\boldsymbol{sp.})}} + \frac{a_3}{1+e^{-a_2(\boldsymbol{sp.})}} * cos(\theta - pd_{sp}) + a_4 * cos\left(\theta - pd_{sp} - \frac{a_5}{1+e^{-a_2(\boldsymbol{sp.})}}\right) + c_1$$

with constants a_1, a_2, a_3, a_4, a_5.

We fitted neuronal activity with these four models (MATLAB 'fit' function), and compared the fitting goodness with adjusted R-squares ($R^2_{adj.} = \frac{(1-r^2)(n-1)}{n-p-1}$, where n is the trial number, and p is the degree of the polynomial).

Simulation with model neurons were based on three models to investigate the relationship between neuronal tuning and population neural geometry (Fig. 5b). We first built three model neuron groups (each n=200) and performed PCA to get the neural state (Fig. 5c). Then, we repeated this in a mixed group, with 100 each of PD shift, gain and addition model neurons (Fig. 5d). Model neurons had three components: cosine-tuning for reach direction ($\theta_{pd,n}$, PD uniform distribution around circle for each neuron n), Gaussian temporal profiles (t=1:200, σ=30, peak time $t_{\mu,n} \in N(100, 10)$, the 100-th bin is MO, random distribution for $t_{\mu,n}$ of neurons), and distinct target-motion modulation for each group. We designed five target speed values ($sp. = [1,2,3,4,5]$) and 64 reach directions ($\theta = 360 * \frac{[1:64]}{64}$), for 320 trials in total[59].

The gain-model neuron has a nonlinear function with target-speed effects on the amplitude:

$$FR_{t,n,sp.,\theta} = e^{\frac{-(t-t_{\mu,n})^2}{2*30^2}} * \left(\frac{1}{1+e^{-g_n(sp.-3)}} * cos(\theta - \theta_{pd,n}) + 1\right)$$

where g_n is a random target-motion gain within [0:1] for different neuron, and modulates target-motion gain in a sigmoidal function.

The PD-shift model neuron has target-speed change in PD:

$$FR_{t,n,sp.,\theta} = e^{\frac{-(t-t_{\mu,n})^2}{2*30^2}} * \left(cos\left(\theta - \theta_{pd,n} - \frac{90}{1+e^{-s_n(sp.-3)}}\right) + 1\right)$$

where s_n is a random value within [0:1.5] for different neuron, and contributes to a sigmoidal function with target-motion shift on neuronal PD ($\theta_{pd,n}$).

The addition model neuron has target-speed effects in offset:

$$FR_{t,n,sp.,\theta} = e^{\frac{-(t-t_{\mu,n})^2}{2*30^2}} * \left(cos\left(\theta - \theta_{pd,n}\right) + \frac{1}{1+e^{-g_n(sp.-3)}} + 1\right)$$

where g_n is also a random value within [0:1] for different neuron, and adjusts the offset activity in a sigmoidal function with target-motion.

The firing rates of three groups model neuron (K*N*T, 320*200*200) were averaged at MO (mean T = [50:150]) to get K*N (320*200) dataset for PCA. Similar to real neural data, we selected the first three PC of K*C (320*200) to show the neural state.

RNN training

For the inputs of RNN, motor intention appeared from MO-50 ms to MO, and was represented as constant variables in the form of two-dimensional Cartesian coordinates; target location was designed as time varying two-dimensional Cartesian coordinates of target throughout the entire trial; the Go-signal was a step function jumping from 0 to 1 at GO. The RNN consisted of 200 hidden units, and output hand velocity for accurate interception after MO.

The RNN nodes evolved according to a standard dynamic differential equation:

$$\tau\dot{x} = -x + Jr + Bu$$

where τ is a time constant (here 50 ms), x is the activity, r is the firing rates, and u means the combined inputs. The connection matrix J of hidden layer is initiated as random in a normal distribution (mean = 0, sigma = $g/\sqrt{N}$, g = 1.5, N = 200), and the matrix B denotes the connection between inputs and hidden units, initiated as zero matrix. The output z is obtained by

$$z = Wr$$

where W is the read-out weight, and is expected to reproduce the desired hand velocity generated by bell-shaped physical equation[60]. W was also initiated as zero matrix. During training, the loss function was:

$$E = e + \alpha r_1$$

where e is the mean squared error of z and training target. r_1 is regularity [61], denoting the magnitude of the nodes' activity and is calculated as activity squared sum through time. For constants, $\alpha = 1e - 7$. The optimization was realized with Adam based on PyTorch, the learning rate was 0.001.

The classification of nodes' modulation type was finished with the same procedure for real data as above. When silencing certain type of modulations, all connections of the nodes of the selected modulation were set to zero; when blocking the connection between certain types of modulations, the selected connection was set to zero. These perturbations were retained for the entire trial. The perturbed networks were tested with the same test set of 500 trials as for the intact network.

Data availability

The datasets and code supporting the current study have not been deposited in a public repository but are available from the corresponding author He Cui (hecui@cibr.ac.cn) on request.

References

1. Evarts, E. V. Relation of pyramidal tract activity to force exerted during voluntary movement. *J. Neurophysiol.* **31**, 14–27 (1968).
2. Tanaka, H. Modeling the motor cortex: Optimality, recurrent neural networks, and spatial dynamics. *Neurosci. Res.* **104**, 64–71 (2016).

3. Georgopoulos, A., Kalaska, J., Caminiti, R. & Massey, J. On the relations between the direction of two-dimensional arm movements and cell discharge in primate motor cortex. *J. Neurosci.* **2**, 1527–1537 (1982).
4. Omrani, M., Kaufman, M. T., Hatsopoulos, N. G. & Cheney, P. D. Perspectives on classical controversies about the motor cortex. *J. Neurophysiol.* **118**, 1828–1848 (2017).
5. Wang, T., Chen, Y. & Cui, H. From Parametric Representation to Dynamical System: Shifting Views of the Motor Cortex in Motor Control. *Neurosci. Bull.* (2022) doi:10.1007/s12264-022-00832-x.
6. Rizzolatti, G., Scandolara, C., Matelli, M. & Gentilucci, M. Afferent properties of periarcuate neurons in macaque monkeys. II. Visual responses. *Behav. Brain Res.* **2**, 147–163 (1981).
7. Lamarre, Y., Busby, L. & Spidalieri, G. Fast ballistic arm movements triggered by visual, auditory, and somesthetic stimuli in the monkey. I. Activity of precentral cortical neurons. *J. Neurophysiol.* **50**, 1343–1358 (1983).
8. Merchant, H., Battaglia-Mayer, A. & Georgopoulos, A. P. Effects of Optic Flow in Motor Cortex and Area 7a. *J. Neurophysiol.* **86**, 1937–1954 (2001).
9. Merchant, H., Battaglia-Mayer, A. & Georgopoulos, A. P. Neural responses in motor cortex and area 7a to real and apparent motion. *Exp. Brain Res.* **154**, 291–307 (2004).
10. Rao, N. G. & Donoghue, J. P. Cue to action processing in motor cortex populations. *J. Neurophysiol.* **111**, 441–453 (2014).
11. Hatsopoulos, N. G. & Suminski, A. J. Sensing with the Motor Cortex. *Neuron* **72**, 477–487 (2011).
12. Sobinov, A. R. & Bensmaia, S. J. The neural mechanisms of manual dexterity. *Nat. Rev. Neurosci.* **22**, 741–757 (2021).
13. Pesaran, B., Nelson, M. J. & Andersen, R. A. Dorsal Premotor Neurons Encode the Relative Position of the Hand, Eye, and Goal during Reach Planning. *Neuron* **51**, 125–134 (2006).
14. Paninski, L., Fellows, M. R., Hatsopoulos, N. G. & Donoghue, J. P. Spatiotemporal Tuning of Motor Cortical Neurons for Hand Position and Velocity. *J. Neurophysiol.* **91**, 515–532 (2004).
15. Cisek, P. & Kalaska, J. F. Neural Correlates of Reaching Decisions in Dorsal Premotor Cortex: Specification of Multiple Direction Choices and Final Selection of Action. *Neuron* **45**, 801–814 (2005).
16. Tkach, D., Reimer, J. & Hatsopoulos, N. G. Congruent Activity during Action and Action Observation in Motor Cortex. *J. Neurosci.* **27**, 13241–13250 (2007).
17. Churchland, M. M. *et al.* Neural population dynamics during reaching. (2012) doi:10.1038/nature11129.
18. Shenoy, K. V, Sahani, M. & Churchland, M. M. Cortical Control of Arm Movements: A Dynamical Systems Perspective. *Annu. Rev. Neurosci.* **36**, 337–359 (2013).
19. Vyas, S., Golub, M. D., Sussillo, D. & Shenoy, K. V. Computation Through Neural Population Dynamics. *Annu. Rev. Neurosci.* **43**, 249–275 (2020).
20. Churchland, M. M., Yu, B. M., Ryu, S. I., Santhanam, G. & Shenoy, K. V. Neural Variability in Premotor Cortex Provides a Signature of Motor Preparation. **26**, 3697–3712 (2006).
21. Churchland, M. M., Cunningham, J. P., Kaufman, M. T., Ryu, S. I. & Shenoy, K. V. Cortical Preparatory Activity: Representation of Movement or First Cog in a Dynamical Machine? *Neuron* **68**, 387–400 (2010).
22. Merchant, H., Battaglia-Mayer, A. & Georgopoulos, A. P. Neural Responses during Interception of Real and Apparent Circularly Moving Stimuli in Motor Cortex and Area 7a. *Cereb. Cortex* **14**, 314–331 (2004).
23. Li, Y., Wang, Y. & Cui, H. Posterior parietal cortex predicts upcoming movement in dynamic sensorimotor control. *Proc. Natl. Acad. Sci.* **119**, e2118903119 (2022).
24. Li, Y., Wang, Y. & Cui, H. Eye-hand coordination during flexible manual interception of an abruptly appearing, moving target. *J. Neurophysiol.* **119**, 221–234 (2018).
25. Merchant, H., Battaglia-Mayer, A. & Georgopoulos, A. P. Functional organization of parietal neuronal responses to optic-flow stimuli. *J. Neurophysiol.* **90**, 675–82 (2003).
26. Kwan, H. C., Mackay, W. A., Murphy, J. T. & Wong, Y. C. Properties of visual cue responses in primate precentral cortex. *Brain Res.* **343**, 24–35 (1985).

27. Kruse, W. Temporal Relation of Population Activity in Visual Areas MT/MST and in Primary Motor Cortex during Visually Guided Tracking Movements. *Cereb. Cortex* **12**, 466–476 (2002).
28. Alexander, G. E. & Crutcher, M. D. Neural representations of the target (goal) of visually guided arm movements in three motor areas of the monkey. *J. Neurophysiol.* **64**, 164–178 (1990).
29. Lurito, J. T., Georgakopoulos, T. & Georgopoulos, A. P. Cognitive spatial-motor processes. 7. The making of movements at an angle from a stimulus direction: studies of motor cortical activity at the single cell and population levels. *Exp. Brain Res.* **87**, 562–580 (1991).
30. Port, N. L., Kruse, W., Lee, D. & Georgopoulos, A. P. Motor Cortical Activity during Interception of Moving Targets. *J. Cogn. Neurosci.* **13**, 306–318 (2001).
31. Inoue, Y., Mao, H., Suway, S. B., Orellana, J. & Schwartz, A. B. Decoding arm speed during reaching. *Nat. Commun.* **9**, 1–14 (2018).
32. Moran, D. W. & Schwartz, A. B. Motor Cortical Representation of Speed and Direction During Reaching. *J. Neurophysiol.* **82**, 2676–2692 (1999).
33. Scott, S. H. & Kalaska, J. F. Reaching Movements With Similar Hand Paths But Different Arm Orientations. I. Activity of Individual Cells in Motor Cortex. *J. Neurophysiol.* **77**, 826–852 (1997).
34. Sun, X. *et al.* Cortical preparatory activity indexes learned motor memories. *Nature* **602**, 274–279 (2022).
35. Kaufman, M. T., Churchland, M. M., Ryu, S. I. & Shenoy, K. V. Cortical activity in the null space: permitting preparation without movement. *Nat. Neurosci.* **17**, 440–448 (2014).
36. Stavisky, S. D., Kao, J. C., Ryu, S. I. & Shenoy, K. V. Motor Cortical Visuomotor Feedback Activity Is Initially Isolated from Downstream Targets in Output-Null Neural State Space Dimensions. *Neuron* **95**, 195-208.e9 (2017).
37. Jazayeri, M. & Shadlen, M. N. Temporal context calibrates interval timing. *Nat. Neurosci.* **13**, 1020–1026 (2010).
38. Wang, J., Narain, D., Hosseini, E. A. & Jazayeri, M. Flexible timing by temporal scaling of cortical responses. *Nat. Neurosci.* **21**, 102–110 (2018).
39. Remington, E. D., Narain, D., Hosseini, E. A. & Jazayeri, M. Flexible Sensorimotor Computations through Rapid Reconfiguration of Cortical Dynamics. *Neuron* **98**, 1005–1019 (2018).
40. Sohn, H., Narain, D., Meirhaeghe, N. & Jazayeri, M. Bayesian Computation through Cortical Latent Dynamics. *Neuron* **103**, 934-947.e5 (2019).
41. Kriegeskorte, N. & Wei, X. X. Neural tuning and representational geometry. *Nat. Rev. Neurosci.* **22**, 703–718 (2021).
42. Dubreuil, A., Valente, A., Beiran, M., Mastrogiuseppe, F. & Ostojic, S. The role of population structure in computations through neural dynamics. *Nat. Neurosci.* **25**, 783–794 (2022).
43. Kakei, S., Hoffman, D. S. & Strick, P. L. Muscle and Movement Representations in the Primary Motor Cortex. *Science (80-.).* **285**, 2136–2139 (1999).
44. Kakei, S., Hoffman, D. S. & Strick, P. L. Direction of action is represented in the ventral premotor cortex. *Nat. Neurosci.* **4**, 1020–1025 (2001).
45. Batista, A. P., Buneo, C. a, Snyder, L. H. & Andersen, R. a. Reach Plans in Eye-Centered Coordinates. *Science (80-.).* **285**, 257–260 (1999).
46. Buneo, C. a, Jarvis, M. R., Batista, A. P. & Andersen, R. a. Direct visuomotor transformations for reaching. *Nature* **416**, 632–636 (2002).
47. Chang, S. W. C., Papadimitriou, C. & Snyder, L. H. Using a Compound Gain Field to Compute a Reach Plan. *Neuron* **64**, 744–755 (2009).
48. Andersen, R. A., Snyder, L., Bradley, D. & Xing, J. Multimodal Representation of Space in the Posterior Parietal Cortex and Its Use in Planning Movements. *Annu. Rev. Neurosci.* **20**, 303–330 (1997).
49. Andersen, R. A. & Buneo, C. A. Intentional maps in posterior parietal cortex. *Annu Rev Neurosci* **25**, 189–220 (2002).
50. Cohen, Y. E. & Andersen, R. A. A common reference frame for movement plans in the posterior parietal cortex. *Nat. Rev. Neurosci.* **3**, 553–562 (2002).

51. Andersen, R. A. & Cui, H. Intention, Action Planning, and Decision Making in Parietal-Frontal Circuits. *Neuron* **63**, 568–583 (2009).
52. Battaglia-Mayer, A. & Caminiti, R. Cortico-Cortical Systems Underlying High-Order Motor Control. *J. Neurosci.* **39**, 2094–18 (2019).
53. Schaffelhofer, S. & Scherberger, H. Object vision to hand action in macaque parietal, premotor, and motor cortices. *Elife* **5**, 1–24 (2016).
54. Dann, B., Michaels, J. A., Schaffelhofer, S. & Scherberger, H. Uniting functional network topology and oscillations in the fronto-parietal single unit network of behaving primates. *Elife* **5**, 1–27 (2016).
55. Martínez-Vázquez, P. & Gail, A. Directed interaction between monkey premotor and posterior parietal cortex during motor-goal retrieval from working memory. *Cereb. Cortex* **28**, 1866–1881 (2018).
56. Cui, H. Forward Prediction in the Posterior Parietal Cortex and Dynamic Brain-Machine Interface. *Front. Integr. Neurosci.* **10**, 1–6 (2016).
57. Brozović, M., Gail, A. & Andersen, R. A. Gain mechanisms for contextually guided visuomotor transformations. *J. Neurosci.* **27**, 10588–10596 (2007).
58. Berens, P. CircStat : A MATLAB Toolbox for Circular Statistics. *J. Stat. Softw.* **31**, 128–129 (2009).
59. Michaels, J. A., Dann, B. & Scherberger, H. Neural Population Dynamics during Reaching Are Better Explained by a Dynamical System than Representational Tuning. *PLoS Comput. Biol.* **12**, 1–22 (2016).
60. Kao, T. C., Sadabadi, M. S. & Hennequin, G. Optimal anticipatory control as a theory of motor preparation: A thalamo-cortical circuit model. *Neuron* **109**, 1567-1581.e12 (2021).
61. Sussillo, D., Churchland, M. M., Kaufman, M. T. & Shenoy, K. V. A neural network that finds a naturalistic solution for the production of muscle activity. *Nat. Neurosci.* **18**, 1025–1033 (2015).

Acknowledgements

We thank C. Li, J. Malpeli, C. Zheng, and R. Zheng for helpful comments and discussions; C. Guan for veterinary assistance; and P. Ding, L. Du, and Z. Xiao for administrative support. This work was supported by the National Key R&D Program (Grants 2020YFB1313400 and 2017YFA0701102), National Science Foundation of China (Grants 31871047 and 31671075), and CAS Strategic Priority Research Program (Grant XDB32040103).

Author Contributions

Y. Zhang and H. Cui designed the experiment, Y. Zhang and T. Wang collected the data, Y. Zhang and Y. Chen analyzed the data, Y. Chen built RNNs, Y. Zhang performed the simulation, Y. Zhang, Y. Chen, T Wang, and H. Cui prepared the manuscript.

Funding

This work was supported by National Key R&D Program (Grants 2020YFB1313400 and 2017YFA0701102), National Science Foundation of China (Grants 31871047 and 31671075), Shanghai Municipal Science and Technology Major Project (Grant 2021SHZDZX) and CAS Strategic Priority Research Program (Grant XDB32040103).

The authors declare no competing interests.